MEASUREMENTS OF RADIATING HYPERVELOCITY AIR SHOCK LAYERS IN THE T6 FREE-PISTON DRIVEN SHOCK TUBE.

Peter L. Collen, Luke J. Doherty & Matthew McGilvray

Oxford Thermofluids Institute
Department of Engineering Science
University of Oxford

ABSTRACT

At super-orbital entry velocities into the Earth's atmosphere, radiant heating from the high temperature post-shock gas can form the majority of the peak heat flux on a vehicle surface. This effect scales strongly with flight velocity and vehicle size. This paper presents results from experiments in the T6 free-piston driven shock tube, in which were made measurements of spectrally and spatially resolved radiance behind strong shock waves in air. Data from equilibrium and non-equilibrium regions of the flow-field are given from emission spectroscopy measurements from 350 to $850\,\mathrm{nm}$ and comparisons made to existing data from other facilities as well as to computational tools.

***Index Terms*—** Radiation, Shock Tube, Equilibrium, Lunar Return

1. INTRODUCTION

During atmospheric entry the gas ahead of a vehicle decelerates through a strong shock-wave. This process causes substantial heating of the flow, with temperatures in excess of 10,000K being common for super-orbital entries. This high temperature post-shock gas produces intense electromagnetic radiation, contributing to the net heat flux incident on the vehicle surface. In the case of high velocities, large vehicles or certain atmospheric compositions the heat flux from radiative sources can exceed that due to convection [1]. Quantification of the radiative heat flux is complicated by the presence of both chemical and thermal non-equilibrium in the flow and the inability to apply traditional scaling laws [2]. However, despite the relevance of radiative heating for currently proposed missions these mechanisms are not fully understood. As a result, uncertainties in radiative heating rates are high [3, 4] which directly impacts thermal protection system design margins and consequently mission payloads. Reduction of these uncertainties requires high quality ground test data to validate ab-initio calculations and computational models.

There are several common experimental approaches used to inform chemical kinetic and radiative modelling efforts for entry. Atmospheric plasma torches and arc jets can create steady, high-enthalpy flows and have been used extensively for development of computational tools. However, they do not accurately reproduce the spatial development of the thermochemical state of the post-shock gas, which makes them unsuitable for the assessment of non-equilibrium peak radiation [5]. Accurately capturing the structure of the shock layer requires a transient facility. A common approach, employed by reflected shock tunnels and expansion tubes, uses a test model to establish a similar flow-field to that expected during flight. This flow-field can then be probed through optical techniques or direct measurements made of heat flux via gauges mounted within the model itself. These gauges can be arranged so as to measure only radiative heat flux from specific wavelength regions (e.g. Tanno et al. [6]). Whilst model-based testing can produce useful results, there are several draw-backs which limit the effectiveness of the approach. Firstly,the most common method used to scale test conditions with model size (binary, or ρ-L, scaling) does not accurately capture radiation — ground test results cannot hence be directly applied to the full-scale case. For radiative measurements, reflection from the model surface can reduce data quality at certain wavelength regions. Finally, model tests can experience augmentation of flow-field emission, stemming from high temperature free-stream gas or flow contaminants [7].

Shock tubes provide a means of reproducing the spatial development of radiation behind a shock at true-flight conditions whilst also comprising a relatively simple system. In such experiments, a shock is passed through a quiescent gas mixture. The shock speed — as well as gas pressure and composition — are chosen to match a trajectory point of interest, and are unscaled. An analogy is then made between the normal shock passing down the shock tube and the stagnation line on a flight vehicle. The flow in this case is approximately one-dimensional, greatly simplifying comparisons to numerical tools. In addition, although only strictly capable of producing normal shocks it has recently been proposed that shock tubes could be suitable sources ground test data for other regions of the flow-field, including conditions through oblique shocks further along the forebody and for those relevant to after-body heating [8].

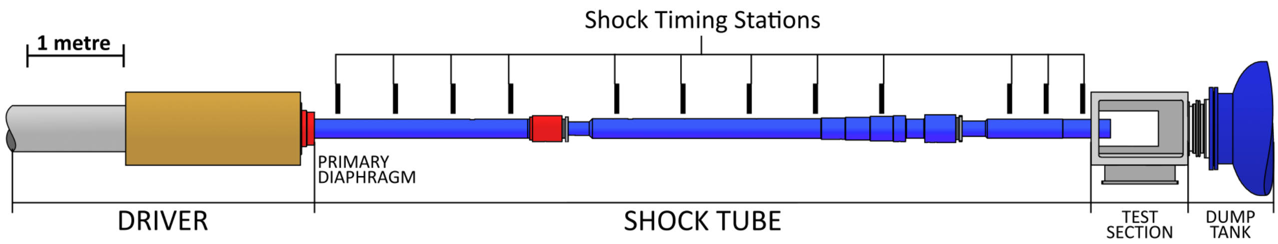

Fig. 1: Diagram of T6 in steel shock tube mode.

Although shock tubes are used extensively for chemical kinetics research, relatively few world-wide are capable of performing super-orbital experiments [5]. As a result, the availability of comparable datasets is limited. Despite the relative simplicity of the shock tube system, factors such as boundary layer absorption, shock speed variation and test gas contamination may significantly impact the observed results [9]. Cross-facility comparisons are therefore essential to differentiate between experimental artefacts and real physical phenomena.

This paper presents data from experimental measurements of lunar return shock layer radiation in the T6 free-piston driven shock tube. A brief description of the facility is first provided, followed by an overview of the experimental apparatus and the calibration procedure. A summary of the tested conditions is then presented, including data on the typical shock speed variation observed. Finally, experimental results are provided alongside a comparison to benchmark data from the NASA Ames Electric Arc Shock Tube (EAST) facility, an atmospheric plasma torch and to computational predictions from NEQAIR.

2. FACILITY DESCRIPTION

T6 is a multi-mode, high enthalpy, transient aerothermodynamic ground test facility. It is capable of operating in four distinct configurations: reflected shock tunnel, expansion tube and two shock tube modes. A more complete overview of the facility history has been given by McGilvray et al. [10] and more recently by Collen et al. [11]. The work detailed in this paper was completed in the steel shock tube mode, and so only a discussion of the details relevant to this experimental campaign is given here.

A diagram of the T6 steel shock tube mode is given in Fig. 1. The driver section is of the Stalker free-piston design [12], wherein a massive piston is used to polytropically compress the driver gas to a desired pressure and temperature. A stainless steel diaphragm — which initially separates the driver gas from the test gas in the shock tube — then ruptures, sending a shock downstream into the test gas. The piston then continues to compress the driver gas, maintaining pressure in the driver section and preventing the generation of expansion waves which would otherwise travel downstream and attenuate the shock. In these experiments, the diaphragm was $0.9\,\mathrm{mm}$ stainless steel and the driver gas pure helium. A rupture pressure of $29\,\mathrm{MPa}$ was used with a compression ratio of 60:1, giving a temperature at rupture of approximately $4500\,\mathrm{K}$. The shock tubes have a diameter of $96.3\,\mathrm{mm}$ and an overall length of approximately $8.75\,\mathrm{m}$, measured from the primary diaphragm to the tube outlet in the test section.

Piezoelectric pressure transducers in the tube wall (PCB series 113) are used to measure the post-shock pressure during the test. Their positions are also shown in Fig. 1. In these experiments a single image of the shock is captured as it emerges into the test section. This requires precise timing of the camera gating to successfully image the shock. The signals from the final three shock timing stations are used as inputs to a timing box, which calculates the shock speed in real time to predict shock arrival.

3. EXPERIMENTAL ARRANGEMENT

The experimental results discussed in this work were collected using emission spectroscopy. A diagram of the arrangement used (based on the approach taken in the X2 expansion tube at the University of Queensland [13]) is shown in Fig. 2. In the T6 steel shock tube mode, a single image is taken of the shock as it emerges from the tube. A system of UV-enhanced aluminium mirrors (Thorlabs Series F01) — consisting of a periscope, 100mm focal length spherical mirror and a flat turning mirror — images and rotates by $90°$ an axial line in the test section onto the slit of a Princeton Instruments IsoPlane 320 spectrograph with a demagnification of approximately 11:1. For measurements in the red portion of the spectrum a $550\,\mathrm{nm}$ longpass filter was added to the optical path to prevent second-order interference from shorter wavelengths.

The spectrograph uses a diffraction grating to split the incident light by wavelength, resulting in a two-dimensional, spatially- and spectrally-resolved map of intensity variation. This is imaged onto the sensor of an Andor iStar intensified camera, located at the exit plane of the spectrometer. The camera was gated on the order of $500\,\mathrm{ns}$ to capture an image of the shock with minimal spatial blurring. In this

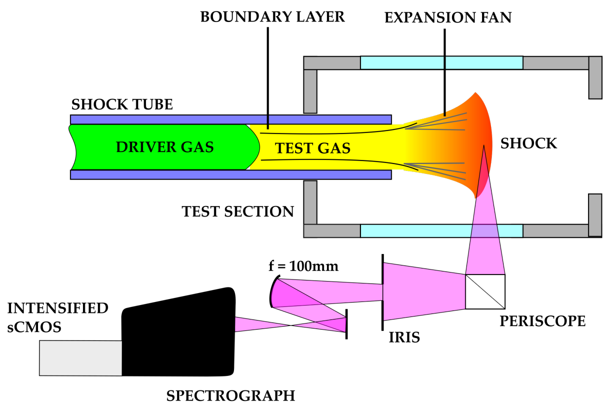

Fig. 2: Diagram of arrangement for shock layer emission spectroscopy experiments.

work, both high and low resolution spectral measurements in the range 350–850 nm were made, respectively using either a $150\,\mathrm{mm}^{-1}$ or $1200\,\mathrm{mm}^{-1}$ grating, both blazed at $500\,\mathrm{nm}$.

3.1. Calibration Procedure

Measurements made using the arrangement shown in Fig. 2 result in a spatially- and spectrally-resolved image taken by the camera — with intensity measured in pixel counts. To translate this result into a meaningful form, a relationship between source brightness and the measured signal on the camera is required. Additionally,the measured intensity is biased by the wavelength-dependent sensitivity of the camera and optical path, as well as by any spatial non-uniformities such as vignetting.

In this work, intensity calibration was performed using a Bentham Instruments SRS8 integrating sphere. The lamp was placed in the test section at the tube centreline; this allowed the entire optical path to be calibrated in-situ, thereby accounting for all system losses. The sphere is a radiant source, and so it is unnecessary to characterise the solid angle subtended by the optical path. The integrating sphere has an outlet diameter of only $50\,\mathrm{mm}$, and so was translated axially (with 50% overlap) to cover the entire field of view. At each point, fifteen images were taken and an average used to minimise the effect of noise on the calibration signal. This calibration procedure was carried out after each test to account for any changes in transmission due to build-up of residue on the interior surface of the test section window. The resulting signal on the camera was then compared to the known source strength of the integrating sphere to allow a value of absolute sensitivity (in units of counts per second per unit spectral radiance, $\mathrm{Counts}\ \mathrm{s}^{-1}$ per $\mathrm{W\,cm^{-2}\,sr^{-1}\,\mu m^{-1}}$), permitting comparison with numerical tools and with other facilities.

The calibration images were taken using the same intensifier gain as employed in the experiments, but a longer exposure time (approximately $400\,\mathrm{\mu s}$) was required due to the dimmer nature of the calibration lamp. The calibration and experimental results must hence be normalised by their respective exposure times. Stray light in the optical system, due to misalignment of the beam path with the entrance of the spectrometer, has been corrected for using the method given by Cruden [14].

Table 1: Parameters for presented test conditions.

Condition	U_s, $\mathrm{km\,s^{-1}}$	P_∞, Pa	Slug Length, mm
High Speed	10.0	26.6	105
Low Speed	7.5	150	282

4. TESTED CONDITIONS

This paper presents data from tests at two Earth return conditions in synthetic air, selected due to the availability of comparison data from other facilities. The specifics of these conditions are given in Table 1. The first ($10.0\,\mathrm{km\,s^{-1}}$ and $26.6\,\mathrm{Pa}$) has been chosen to match a benchmark case from EAST [15], which has undertaken a large number of experiments at this test point. This is a condition typical of lunar return, at which there is expected to be significant presence of non-equilibrium and ionisation effects. The second condition has been selected to give post-shock conditions of approximately $100\,\mathrm{kPa}$ and 6500–7500 K. These are intended to provide comparison with the thesis work of Laux, undertaken in an atmospheric plasma torch [16]. EAST has also performed low speed shots at comparable conditions [17], permitting further comparison of equilibrium radiance with a similar test facility.

As shown in Fig. 2, the slug of test gas which initially occupies the entire length of the shock tube is significantly compressed by the incident shock. The test slug is immediately followed by the driver gas; at this boundary there can be an unknown degree of mixing, leading to contamination of the test gas by the driver. It is therefore desirable to image as far away from this interface as possible to minimise the likelihood of contamination. Table 1 also provides an estimate of the test gas slug length, determined using the method of Mirels [18]. Given that typically only $60\,\mathrm{mm}$ of gas behind the shock is imaged, and that no sign of helium or argon spectral features is apparent in the subsequent data, it is assumed that driver contamination is negligible for the experimental conditions presented here.

As has been previously discussed, radiative phenomena are strongly dependent on shock velocity. Notably, electron densities have been measured as significantly higher than the expected equilibrium values in EAST, an effect attributed to shock deceleration [9]. It is therefore desirable to maintain as

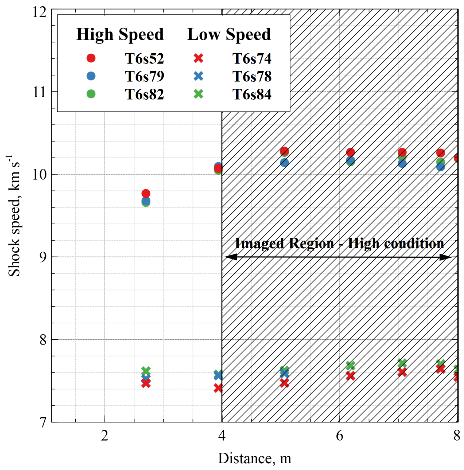

Fig. 3: T6 Shock Tube Mode Shock Speed Variation.

close a shock velocity as possible to the nominal condition in the test gas. Fig. 3 shows representative shock speed variation for the shots presented in this work at both conditions. Also shown is the approximate extent which would be imaged using assuming a $60\,\mathrm{mm}$ length behind the shock at the high condition. It can be seen that the variation in shock speed is small within this region. The observed variability upstream of this area is due to slight differences in diaphragm rupture behaviour which leads to natural shot-to-shot variation. In this work, the quoted shock speeds for a given shot are the average value between the final four shock timing stations. This was deemed valid given the minimal variation in shock velocity through the downstream half of the tube. The averaging process reduces the error bound significantly; overall error on average shock speed is typically on the order of $1\,\%$.

The majority of recent tests in T6 shock tube mode have been undertaken in synthetic air. Despite this, hydrogen lines are still visible in the resulting spectra. The measured leak rate into the volume comprised of the shock tubes, test section and dump tank was measured at better than $1\,\mathrm{Pa\,min^{-1}}$, in line with similar experiments completed in Titan atmospheres [19]. Before each shot, the tube is flushed three times with synthetic air to above $1\,\mathrm{kPa}$, and then pumped down below $5\,\mathrm{Pa}$. Despite this process, hydrogen contaminants are still obvious in many of the measured emission spectra. The source of this contamination is either hydrocarbon residue within the tube or the current level of atmospheric leakage is too high. Investigation into the source is on-going, but it is not expected that the presence of hydrogen will overly influence the spectral results. In the NEQAIR simulations described in Section 5, $1\,\%$ by mole of H2O has been added. This value was chosen to approximately match the experimental results and is included to account for any additional continuum radiation due to electron recombination.

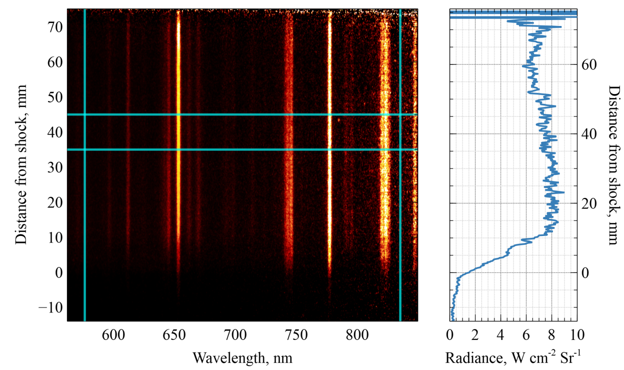

Fig. 4: High condition (T6s52, $10.18\,\mathrm{km\,s^{-1}}$) red spectrum.

5. RESULTS

This section presents spectral results for the two conditions outlined in Section 4. The closest comparable data reported as 'Good' from EAST is also shown in each case. In the equilibrium analysis the results of simulations using NEQAIR v14.0 [20] are also shown. These simulations were undertaken by first performing a shock analysis with the NASA Chemical Equilibrium with Applications code [21] at the measured shock speed. The resulting equilibrium composition was then used as an input to NEQAIR, assuming an optical depth equal to the shock tube diameter ($96.3\,\mathrm{mm}$). All NEQAIR simulations were performed assuming a Boltzmann distribution. Where EAST has been simulated for comparative purposes, the optical depth was assumed equal to the tube diameter of $101.6\,\mathrm{mm}$. In all cases, the equilibrium data is averaged between 35–$45\,\mathrm{mm}$ behind the shock front.

5.1. High Speed Condition

A representative result from an experiment at the high condition in the red spectral region is given in Fig. 4, showing the spatial and spectrally resolved evolution of radiance behind the shock. The vertical and horizontal bars represent the integration limits used to calculate radiance and equilibrium spectral radiance, respectively. Of note is the radiance result in the right of the figure, which shows an inflection in the initial rise due to rapid excitation and subsequent dissociation of molecular species. The radiance is then reasonably constant throughout the shock layer as atomic emission becomes dominant

Figures 5 and 6 show typical equilibrium spectra taken in the range 350–$850\,\mathrm{nm}$. The T6 data shown in Fig. 6 was taken using lab air, but is shown here as it is the closest matching condition to both available EAST benchmark data and Fig. 5. In general, the peak radiance matches reasonably well between T6 and NEQAIR, being less than that shown for the EAST tests. This is likely due in part to differences in opti-

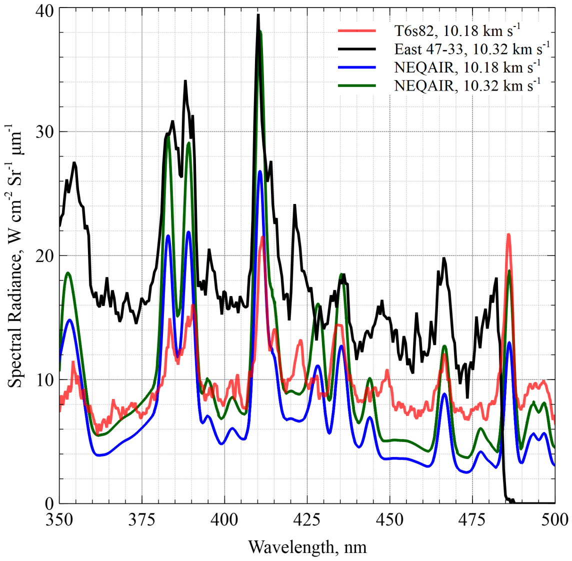

Fig. 5: High speed condition low resolution UV-Vis spectra.

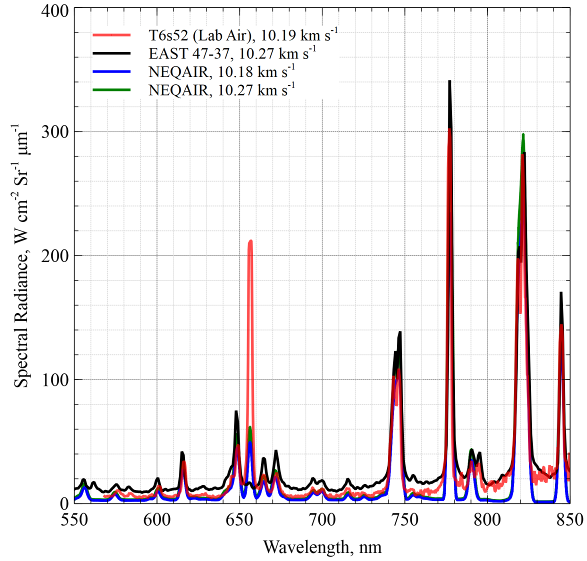

Fig. 6: High speed condition low resolution red spectra.

cal depth and shock speed. A NEQAIR simulation of T6 at the higher velocity of $10.32\,\mathrm{km\,s^{-1}}$ is also shown to demonstrate the influence of the shock speed discrepancy. The background continuum radiation observed in the T6 shock tube experiments is much closer to that measured in EAST and is significantly under-predicted by NEQAIR. The background continuum is made up of electron-driven processes, through both bound-free and free-free mechanisms. A higher-than-anticipated background continuum magnitude has previously also been observed in EAST and X2, where it has been attributed to shock deceleration and hence an electron number density much higher than equilibrium [9]. The magnitude by which the background radiance is observed to be above the nominal in the T6 data falls within this previously observed discrepancy.

To investigate this behaviour further a NEQAIR study was undertaken wherein the electron density was increased. The results of this investigation are shown in Fig. 7. It was found that doubling the electron population gave a much closer match in terms of background radiation. A comparison between the experimental data and the modified simulation is shown in Fig. 7, where a log scale is used to better compare the effects of changes. Although only demonstrated for a single condition the good match between two shots across the UV-NIR range with this modification is encouraging. Curiously, this effect is still observed despite significantly less shock deceleration in T6 when compared to EAST for the data presented here (nominally $0.5\,\%$ over the whole tube in T6 versus $5.0\,\%$ over the imaged region in EAST). Recent work by Chandel et al. [22] has recently demonstrated that boundary layer growth can contribute to increasing electron number density in the test gas. The observation of increased continuum radiance in the T6 data is suggestive that this effect is potentially significant. Further investigation of this hypothesis requires measurements of electron density, which are planned during the next experimental campaign. Comparisons with the T6 aluminium shock tube will also explore this effect further as the influence of boundary layer growth will be lessened due to its larger $225\,\mathrm{mm}$ diameter.

5.1.1. High Resolution Spectra

Fig. 8 shows a high resolution spectrum of atomic nitrogen lines at a centre wavelength of $821\,\mathrm{nm}$. Comparable data from EAST is also shown. It can be observed that the T6 experimental measurements agree reasonably well with NEQAIR, albeit they are over-predicted by approximately $10\,\%$. This discrepancy is due in part to the assumption in the NEQAIR simulations that the optical thickness is equal to the shock tube bore of $96.3\,\mathrm{mm}$. The core flow diameter has not been assessed for T6, but equivalent conditions in the X2 expansion tube determined that the core flow was reduced by $12.5\,\mathrm{mm}$ — $13\,\%$ of the T6 bore. This alone would account for the majority of the observed discrepancy. A NEQAIR simulation of EAST demonstrates the influence of the increased velocity and tube diameter. This comprises the majority of the difference between the two facilities. Comparing this simulation with the EAST experiment shows that NEQAIR under-predicts the experimental result — the opposite trend observed in T6. The cause of this observation is clear in Fig. 9, which shows a comparison between the development of post-shock radiance between EAST and T6 for the equilibrium data of Fig. 8. Also shown as dashed lines are the predicted levels of equilibrium radiance from NEQAIR.

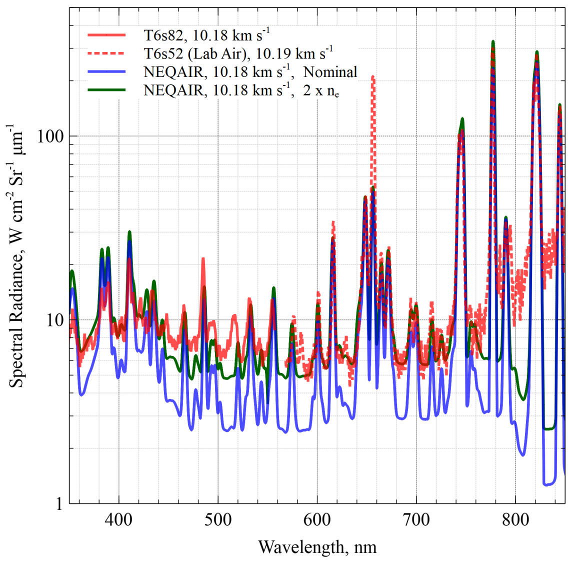

Fig. 7: Influence of changing electron density (n_e) on nominal High speed equilibrium state in NEQAIR.

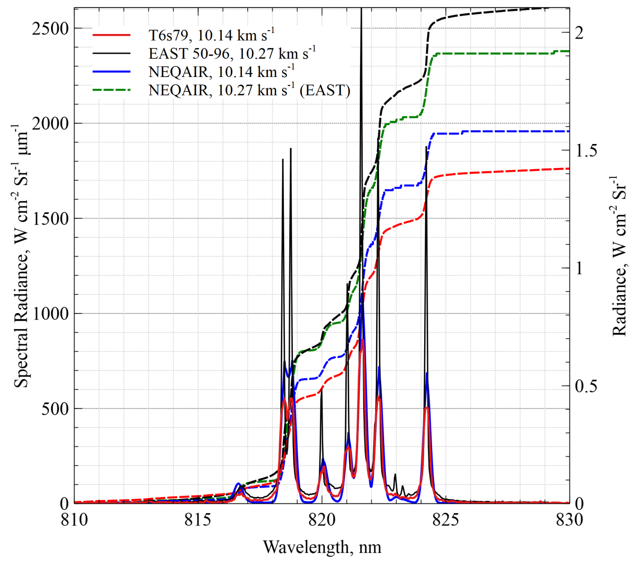

Fig. 8: High speed, high resolution nitrogen spectra. Dashed lines represent cumulative radiance across presented spectral region.

The difference in initial gradient seen in Fig. 9 is due to the camera gate width used, which results in different degrees of spatial blurring. Of interest is the behaviour after the non-equilibrium region: the EAST data continues to rise throughout the post-shock region, whilst T6 shows the opposite trend. This clarifies the differences seen between the two facilities and NEQAIR in Fig. 8. One possible reason for this discrepancy is the large difference in shock deceleration between the two facilities. This effect is thought to result in significant spatial non-uniformities in the test gas slug [9]. Work to fully investigate this effect is on-going.

5.2. Low Speed Condition

An example of the spatio-spectral evolution of radiance in the shock layer at the low condition is shown in Fig. 10. In comparison with Fig. 4, the radiance profile is dominated by molecular emission which leads to a clear non-equilibrium peak. The higher post-shock pressure at this condition should lead to rapid equilibration; this is observed in the experimental results, which exhibit a stable profile throughout the shock layer.

The experimental results from both wavelength regions for the low speed condition are shown in Fig. 11. Also shown is the closest available comparison data from EAST, which have similar shock speed but a lower pressure ($68\,\mathrm{Pa}$ versus $150\,\mathrm{Pa}$). As a result, NEQAIR simulations were run for both T6 and EAST to facilitate comparison. The T6 experiments were designed to give $100\,\mathrm{kPa}$ post-shock pressure, to enable comparison with atmospheric plasma torch data. The thesis data of Laux [16] is also shown in Fig. 11. Given the smaller cross-section of the torch ($50\,\mathrm{mm}$) all data has been normalised by their respective nominal diameter. In addition, the data of Laux was taken at significiantly greater resolution, making comparison of atomic line magnitudes challenging. Here, this data has been convolved with the Gaussian slit function used in the T6 experiments. This is not expected to introduce significant error due to the large difference in instrument function widths.

In general, there is good agreement between the NEQAIR prediction, the data of Laux and the results from T6. As NEQAIR incorporates part of the Laux data agreement between the two is unsurprising, but it does serve to validate the computational results. In the red region the atomic peaks are matched well, as is the background radiance. Whilst the T6 data does appear noisier above approximately $800\,\mathrm{nm}$ it can be seen to track the NEQAIR prediction closely. The Laux plasma torch data slightly exceeds the other experimental results in oxygen atomic emission at $777\,\mathrm{nm}$. Laux found this line to be optically thick at these conditions; the normalisation of spectral radiance by diameter is only strictly valid for optically thin emission and so leads to an apparently greater emission for the smaller plasma torch.

The central region of the UV-Vis spectrum also compares favourably. There is a slight departure of the T6 experimental data above the predicted level in the central visible region (500–$650\,\mathrm{nm}$) which spans the two plots. As discussed in Section 3.1, this optical set-up exhibits some degree of stray light. Whilst this is negligible in regions of brighter signal it has greater influence where radiance is low. A full uncertainty analysis which captures this effect is required to bound

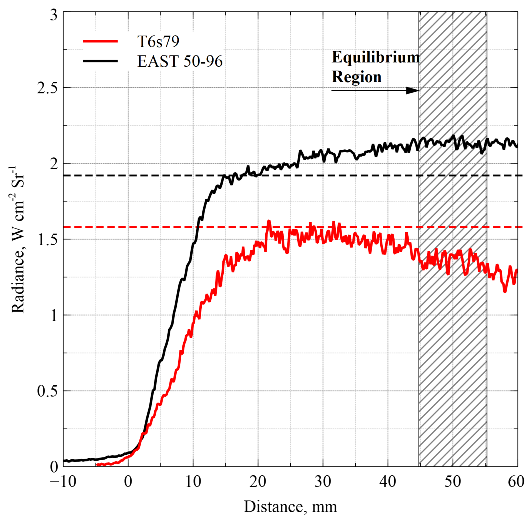

Fig. 9: Comparison of the development of post-shock radiance in T6 and EAST at the High condition. Dashed lines represent equilibrium NEQAIR predictions.

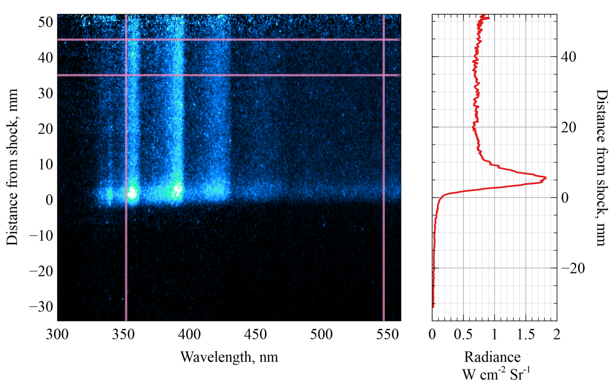

Fig. 10: Low condition (T6s84, $7.69\,\mathrm{km\,s^{-1}}$) UV-Visible spectrum.

the experimental data. Finally, the NEQAIR prediction and experimental data also diverge below around $375\,\mathrm{nm}$. There is a better agreement between the EAST and T6 facilities here, but this is likely co-incidence; instead, it is thought that the reduction in intensity in the T6 data is a calibration artefact due to the low intensity of the integrating sphere in this region.

The good agreement between experiment and computation is not seen when comparing the EAST results and the simulations — it is not currently clear why this would be case. The observed discrepancy does appear to agree with the trends presented in Cruden and Brandis [17], who compared NEQAIR results using differing rate chemistries in the non-equilibrium region of shocks at similar conditions. The trends shown suggest under-prediction of radiance in the equilibrium region, in line with the results shown here.

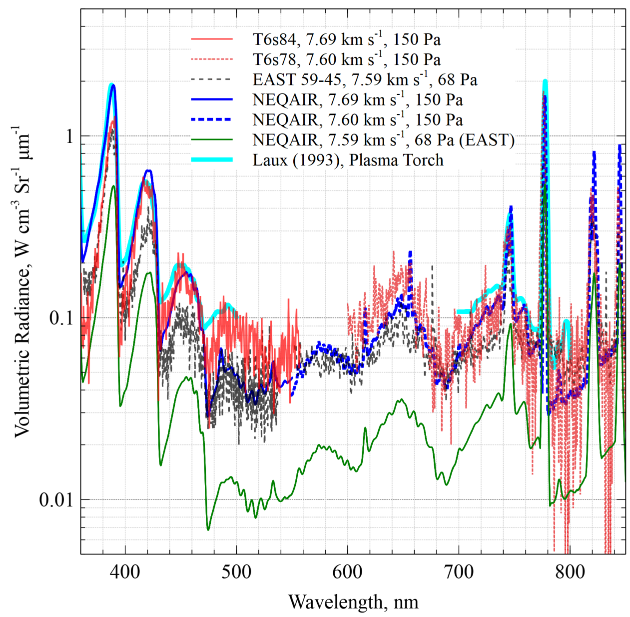

Fig. 11: Low condition equilibrium spectra comparison.

6. CONCLUSIONS & FUTURE WORK

This paper has presented results from shock layer emission spectroscopy experiments at two conditions relevant to lunar return. These experiments were performed in the recently-commissioned T6 free-piston driven shock tube. Good agreement is found between the data from T6 and that from the Electric Arc Shock Tube at NASA Ames. In the case of the higher speed condition at $10\,\mathrm{km\,s^{-1}}$ comparisons to NEQAIR drew similar conclusions to previous studies, wherein the background radiance was found to be under-predicted. Increasing the electron density by a factor of two was found to largely address this discrepancy. For the low speed condition, very good agreement is seen between T6, plasma torch experiments by Laux and the NEQAIR prediction in the equilibrium region. This is not the case for the EAST data available. Future work will perform numerical simulations of the non-equilibrium region to compare exiting rate models to the T6 data.

7. ACKNOWLEDGEMENTS

The authors would like to acknowledge Jim Merrifield and Arthur Smith at Fluid Gravity Engineering for providing funding and support for this work, Brett Cruden and Aaron Brandis for their helpful advice, and Tobias Hermann for his help with the camera set-up and interesting discussions.

8. REFERENCES

[1] A. M. Brandis and C. O. Johnston, "Characterization of stagnation-point heat flux for earth entry," in *45th AIAA Plasmadynamics and Lasers Conference*, 2014.

[2] A. Andrianatos, D. Gildfind, and R. Morgan, "A study of radiation scaling of high enthalpy flows in expansion tubes," in *7th Asia Pacific International Symposium on Aerospace Technology*, 2015.

[3] C. O. Johnston, A. Mazaheri, P. Gnoffo, B. Kleb, and D. Bose, "Radiative heating uncertainty for hyperbolic Earth entry, Part 1: Flight simulation modeling and uncertainty," *Journal of Spacecraft and Rockets*, vol. 50, no. 1, pp. 19–38, 2013.

[4] C. Johnston, A. Brandis, and K. Sutton, "Shock layer radiation modeling and uncertainty for Mars entry," in *43rd AIAA Thermophysics Conference*, 2012, p. 2866.

[5] P. Reynier, "Survey of high-enthalpy shock facilities in the perspective of radiation and chemical kinetics investigations," *Progress in Aerospace Sciences*, vol. 85, pp. 1–32, 2016.

[6] H. Tanno, T. Komuro, K. Sato, K. Itoh, R. P. Lillard, J. Olejniczak, and J. H. Grinstead, "Aeroheating measurement of Apollo shaped capsule with boundary layer trip in the free-piston shock tunnel HIEST," in *52nd Aerospace Sciences Meeting*, 2014, p. 0434.

[7] B. A. Cruden, A. M. Brandis, J. H. Grinstead, J. Olejniczak, L. Kirk, R. P. Lillard, H. Tanno, and T. Komuro, "Measurement of Ultraviolet Radiative Heating Augmentation in HIEST Reflected Shock Tunnel," in *45th AIAA Thermophysics Conference*, 2015, p. 2512.

[8] C. O. Johnston, "Evaluating Shock-Tube Informed Biases for Shock-Layer Radiative Heating Simulations," in *AIAA Aviation 2019 Forum*, 2019, p. 3259.

[9] A. Brandis, B. Cruden, D. Prabhu, D. Bose, M. McGilvray, and R. Morgan, "Analysis of air radiation measurements obtained in the EAST and X2 shocktube facilities," in *10th AIAA/ASME Joint Thermophysics and Heat Transfer Conference*, 2010.

[10] M. McGilvray, L. J. Doherty, R. G. Morgan, D. Gildfind, P. Jacobs, and P. Ireland, "T6: The Oxford University Stalker Tunnel," in *20th AIAA International Space Planes and Hypersonic Systems and Technologies Conference*, 2015.

[11] P. L. Collen, L. Doherty, M. McGilvray, I. Naved, R. T. Penty Geraets, T. A. Hermann, R. G. Morgan, and D. Gildfind, "Commissioning of the T6 Stalker Tunnel," in *AIAA Scitech 2019 Forum*, 2019.

[12] R. J. Stalker, "The Free Piston Shock Tube," *Aeronautical Quarterly*, vol. 17, pp. 351–370, 1966.

[13] R. Morgan, T. McIntyre, R. Gollan, P. Jacobs, A. Brandis, M. McGilvray, D. Van Diem, P. Gnoffo, M. Pulsonnetti, and M. Wright, "Radiation measurements in nonreflected shock tunnels," in *25th AIAA Aerodynamic Measurement Technology and Ground Testing Conference*, 2006.

[14] B. A. Cruden, "Absolute radiation measurements in earth and mars entry conditions," Tech. Rep., NASA, 2014.

[15] A. M. Brandis and B. A. Cruden, "Benchmark Shock Tube Experiments of Radiative Heating Relevant to Earth Re-entry," in *55th AIAA Aerospace Sciences Meeting*, 2017.

[16] C. O. Laux, *Optical Diagnostics and Radiative Emission of Air Plasmas*, Ph.D. thesis, STANFORD UNIVERSITY., 1993.

[17] B. A. Cruden and A. M. Brandis, "Measurement and Prediction of Radiative Non-equilibrium for Air Shocks Between 7-9 km/s," in *AIAA Aviation Forum*, 2017.

[18] H. Mirels, "Test Time in Low-Pressure Shock Tubes," *The physics of Fluids*, vol. 6, no. 9, pp. 1201–1214, 1963.

[19] A. M. Brandis, R. G. Morgan, T. J. McIntyre, and P. A. Jacobs, "Nonequilibrium radiation intensity measurements in simulated Titan atmospheres," *Journal of Thermophysics and Heat Transfer*, vol. 24, no. 2, pp. 291–300, 2010.

[20] B. A. Cruden and A. M. Brandis, "Updates to the NEQAIR radiation solver," Tech. Rep., NASA, 2014.

[21] B. J. McBride and S. Gordon, "Computer Program for Calculation of Complex Chemical Equilibrium Compositions and Applications: II. Users Manual and Program Description," NASA Reference Publication NASA RP 1311, NASA Lewis Research Center, Cleveland, OH, 1996.

[22] D. Chandel, I. Nompelis, G. V. Candler, and A. M. Brandis, "CFD Predictions of High Enthalpy Shocks in Nitrogen," in *AIAA Aviation 2019 Forum*, 2019, p. 3078.